Check for updates

www.lpr-journal.org

Solution-Processed Disordered Plasmonic Surfaces as Optics for Infrared Imaging

Jyotirmoy Mandal,* John Brewer, Sagar Mandal, Robert Yang, and Aaswath P. Raman*

In recent years, thermal imaging and sensing technologies have seen dramatic increases in usage for a range of applications. However, the material cost and manufacturing complexity of infrared optics remain a major barrier toward their democratization. Here, a solution-processed plasmonic reflective filter (PRF) is presented as a scalable, disordered, and low-cost thermal infrared (TIR) optic. The PRF selectively absorbs sunlight and specularly reflects TIR wavelengths, with a performance comparable to state-of-the-art infrared optics made of materials like Germanium. Unlike the latter, however, the PRF is fabricated using low-cost materials and a "dip-and-dry" chemical synthesis technique, which enables orders of magnitude lower manufacturing costs. The PRF's optical functionality and integration into infrared imaging systems are experimentally demonstrated. The chemical synthesis technique also affords exceptional spectral tuneability and material compatibility compared to traditional fabrication methods. The PRF's tuneable and broadband TIR yield can be augmented by inexpensive dielectric or polymeric filters to yield novel capabilities such as wide-area ambient temperature surveys. Practically, the PRF represents a significant advance toward democratizing the benefits of thermal imaging and sensing. Scientifically, it represents a previously unexplored optical functionality of disordered materials, and a new direction for versatile chemical synthesis in designing optical components.

J. Mandal, J. Brewer, R. Yang, A. P. Raman Department of Materials Science and Engineering University of California Los Angeles, USA E-mail: jm3136@princeton.edu; aaswath@ucla.edu

J. Mandal
Department of Civil & Environmental Engineering

Princeton University Princeton, USA S. Mandal

Independent Researcher Seattle, USA

The ORCID identification number(s) for the author(s) of this article can be found under https://doi.org/10.1002/lpor.202400256

© 2024 The Author(s). Laser & Photonics Reviews published by Wiley-VCH GmbH. This is an open access article under the terms of the Creative Commons Attribution-NonCommercial-NoDerivs License, which permits use and distribution in any medium, provided the original work is properly cited, the use is non-commercial and no modifications or adaptations are made.

DOI: 10.1002/lpor.202400256

1. Introduction

Infrared imaging, also known as thermography or "heat vision", offers a radically different view of the world from what we see. Human eyes and traditional cameras sense radiation in the \approx 0.4–0.7 µm wavelengths (λ), where light from the sun and artificial sources, and the high optical transmittance of the atmosphere, enable imaging of our environment. A similar phenomenon occurs in certain bands within the thermal infrared wavelengths (TIR, $\lambda \approx 2.5-50 \,\mu\text{m}$), including the long-wave infrared band (LWIR, $\lambda = 8-13 \mu m$), where the atmosphere transmits thermal radiation emanating from objects, allowing them to be imaged. Just as our vision informs us about the textures and colors of objects, thermography provides information about their emittances and temperatures, offering an alternative way to optically distinguish objects, or in the absence of illumination, be the sole imaging platform.

Because thermography enables the detection, imaging, and characterization of heat from our surroundings, it is used in diverse applications such as astronomy, atmospheric monitoring, defense, industrial quality control, thermal fault detection (e.g., in building insulation), heat sensing in autonomous vehicles, and medical screening. The last of these applications was recently prominent in the context of the COVID-19 pandemic. However, state-of-the-art thermal cameras contain optical components made from costly materials and require technical finesse to manufacture. Consequently, the use of thermography has historically been limited to high-end consumers. Making thermal imaging a more accessible and affordable technology could significantly impact applications in a wide range of industries, and lead to beneficial uses that are today limited due to the costs of conventional thermographic systems.

The limited accessibility and affordability of thermal imaging and sensing systems arise in large part from the material and fabrication costs of their optical components. Typically, these systems require the filtering of solar heat and direction of TIR radiation onto a sensor, with an additional requirement of specular yield in the TIR for imaging systems. Traditionally, IR-imaging and sensing systems have achieved this using germanium-based transmission optics. A semiconductor with a band-gap of 0.66 eV, germanium (Ge) intrinsically absorbs and filters out noise in

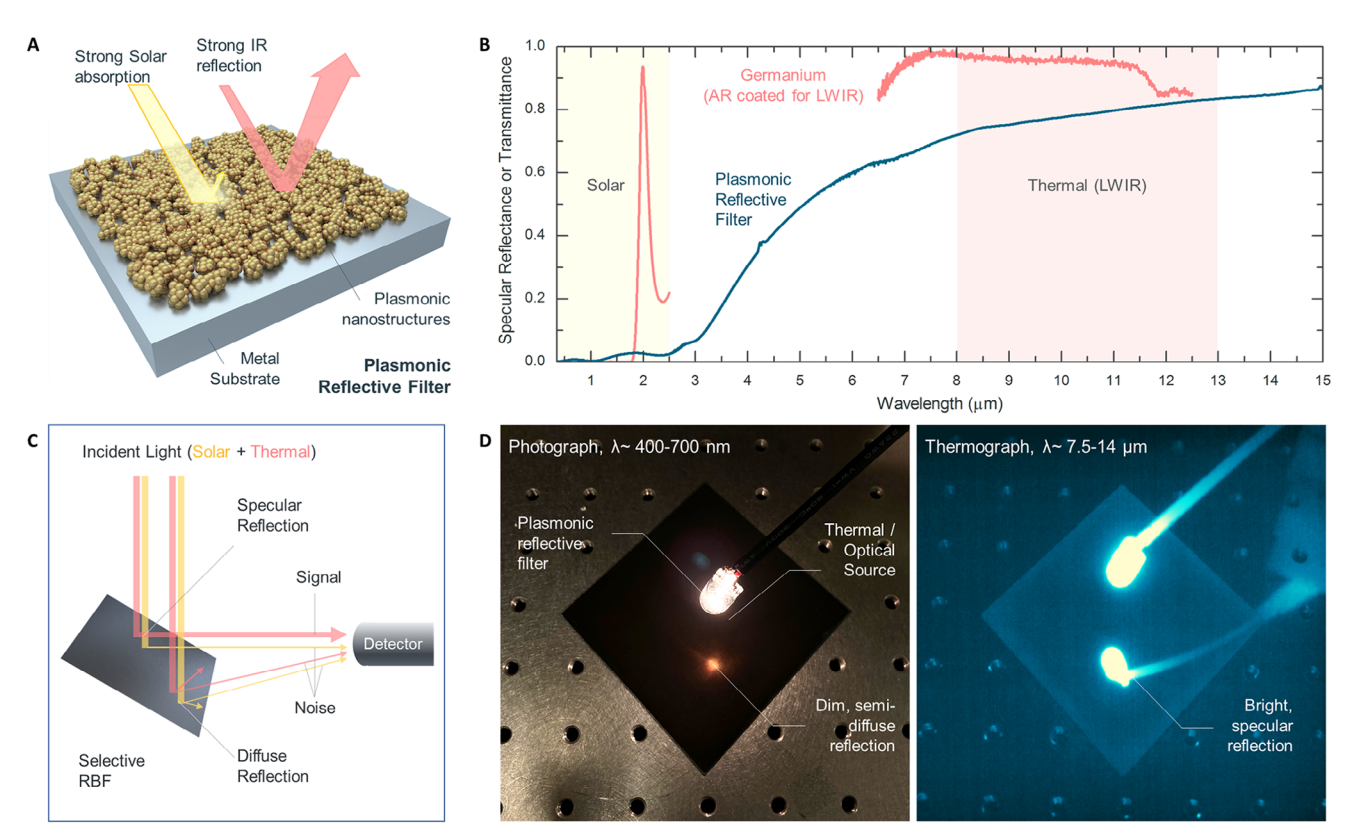


Figure 1. The plasmonic reflective filter (PRF) and its functionality. A) Schematic of the PRF, showing a plasmonic nanostructure-coated metal substrate that acts as a selective reflector of thermal infrared (TIR) radiation. B) Experimentally measured specular reflectance of the PRF presented alongside the transmittance of an antireflection-coated (for LWIR) germanium window for comparison. The transmittance of a bare Ge window is shown in Figure S2 (Supporting Information). As evident, the PRF shows very little shortwave ($\lambda < 2.5 \,\mu\text{m}$) specular reflection, and a high specular reflection across the TIR, particularly in the long-wave infrared (LWIR, $\lambda = 8-13 \,\mu\text{m}$) wavelengths where the atmosphere is transparent. C) Consequently, the PRF can minimize incident noise in the form of sunlight, and direct thermal signatures from the environment onto imaging sensors or detectors, as evident from D) photoand thermographs of a tungsten lamp over a PRF, showing visible absorption and TIR reflection.

the solar wavelengths <1.9 µm, while transmitting longer wavelengths up to 16 μm onto detectors. However, as a material, Ge is expensive, and fashioning its brittle form into precision optical components requires advanced manufacturing processes. Furthermore, the high infrared refractive index (≈4) of Ge requires antireflection coatings on its surfaces to maximize TIR transmission. These factors make Ge-based optics comparatively difficult and expensive to manufacture. Ge-based optics also have operational limitations. For instance, its transmittance at $\lambda \approx 1.9$ – 2.5 µm solar wavelengths^[1,2] lets in noise. Its transmittance also falls and becomes non-monotonic midway through the LWIR at $\lambda \approx 11.5 \ \mu m^{[1,2]}$ – which could complicate radiometric measurements. Furthermore, the increase in intrinsic carrier density with temperature makes Ge's transmittance and dispersion sensitive to temperature, further compounding radiometric measurements, and renders it opaque above 80 °C, preventing its use in high-temperature settings.^[3,4]

Beyond Ge, recent advances in chalcogenide glasses and diffractive lenses are promising, however, they are subject to one or more of the above limitations.^[5–9] Alternatives like polymer, zinc selenide (ZnSe), silicon lenses, or gold-coated reflective surfaces have lower costs and wider transmittance or reflectance bands, but do not adequately filter sunlight. Thus, there remains

considerable room for improvement in terms of cost, fabricability, and optical performance – with the first two being crucial for increasing the scope of, or access to, thermography. One way of achieving this may be through the use of non-traditional optical components in thermal imaging and sensing systems.

In this report, we present a solution-processed plasmonic reflective filter (PRF) as a highly effective optical component for use in thermal imaging systems. Our design consists of a layer of disordered plasmonic metal nanoparticles deposited on a metal surface through a rapid, low-cost process (Figure 1A), which behaves as an efficient specular reflector of incident TIR radiation ($\lambda > 2.5 \mu m$) while emitting little of its own, and strongly absorbing incident shortwave radiation (λ < 2.5 µm) (Figure 1B). The spectrally selective, specular reflectance allows the PRF to direct thermal signatures from objects onto infrared sensors effectively, while filtering out shortwave noise (e.g., sunlight) (Figure 1C,D). We first theoretically explore the optical mechanism that leads to the functionality of the PRF, and then demonstrate a PRF made using an exceptionally scalable solution-based "dip-and-dry" technique, whose optical functionality is verified through spectrophotometry and Twyman-Green interferometry. We then show the integrability of the PRF into existing thermal imaging and sensing systems through

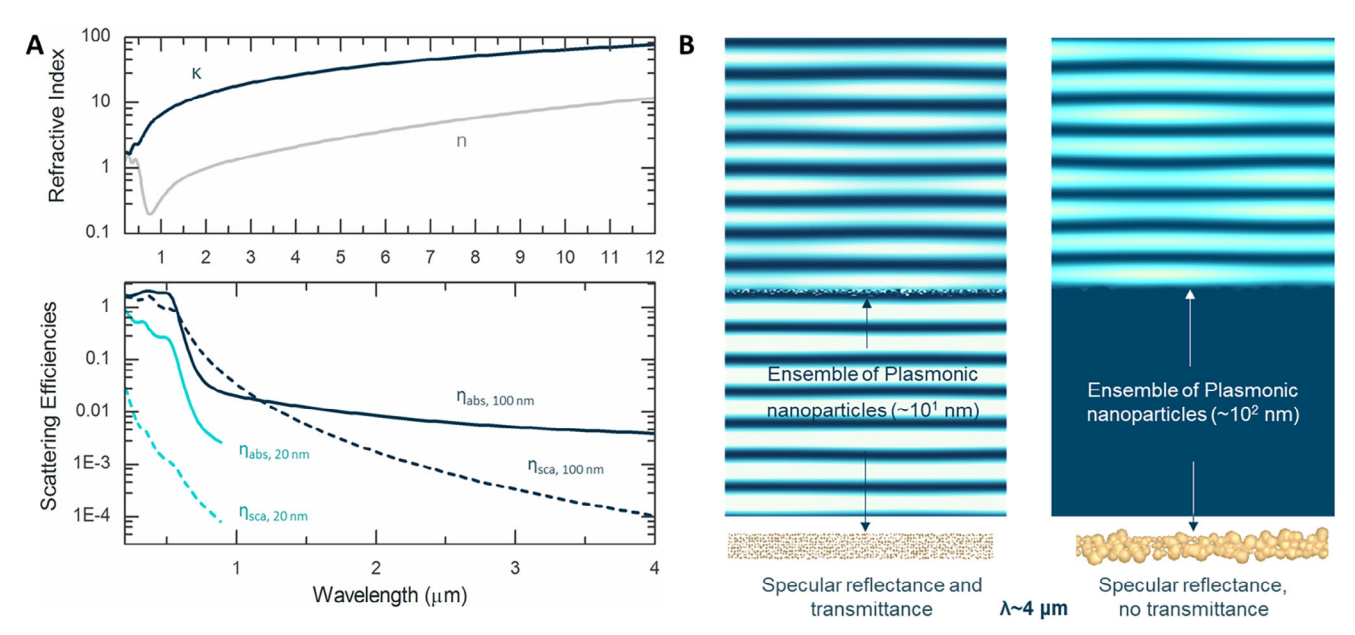


Figure 2. Physical mechanisms behind the plasmonic reflective filter. A) In the case of copper (upper panel), plasmonic nanoparticles, with diameters of 20–100 nm, have relatively high scattering and absorption coefficients in the shorter wavelengths, which diminishes to near-insignificant levels in the longer wavelengths (lower panel). The higher scattering and absorption efficiencies in the shorter wavelengths indicate the ability of the nanoparticles to trap and absorb sunlight efficiently. The higher absorption efficiency (arising from the extinction coefficient) of the particles when their sizes are $<<\lambda$ indicates that a collection of plasmonic nanoparticles would behave as a lossy or potentially reflective effective medium in the thermal infrared wavelengths. B) FDTD simulations of the square of the electric field for a layer of disordered plasmonic nanoparticles under a plane wave ($\lambda = 4 \mu m$) incident from the top. (Left) The ensemble of nanoparticles with sizes \approx 100 nm and fill fraction of 0.4 both specularly reflect and transmit TIR, while (Right) an ensemble of nanoparticles with sizes \approx 100 nm and fill fraction of 0.7 specularly reflect, but do not transmit TIR. Schematics of the respective ensembles used are shown below for each simulation. The results indicate that when placed on a metal substrate, a collection of plasmonic nanoparticles will act as a specular thermal infrared reflector, which is necessary for imaging. It should be noted here that the 2D simulations presented here are adequate to show the general concept we propose. Further details are provided in the SI, Section 2.

radiometric characterizations, compare its performance relative to Germanium (Ge)-based designs used in today's infrared (IR) imaging and sensing systems, and show its spectral tunability and enhancement with polymeric materials. Our work shows that the PRF can yield a state-of-the-art, tunable, and versatile optical performance, but at material and fabrication costs that are $\approx\!100\!-\!1000x$ lower than those of Ge-based optics. From a practical standpoint, this may represent a significant advance in the development of high-performance and low-cost substitutes for Ge-based optics in thermal imagers and sensors. Scientifically, the PRF represents a novel functionality of disordered materials, and opens a new avenue to non-traditional fabrication pathways that combine optics with chemical synthesis.

2. Results

2.1. Theory

Optical components used in IR-imaging and sensing systems must direct incident TIR radiation onto a detector, [10–12] while filtering out sunlight which would otherwise be registered as noise. Typically, the detection occurs in the atmospheric transmission windows, such as the long-wave infrared band (LWIR, λ = 8–13 µm), where thermal emissions from typical terrestrial objects peak, or the mid-wave infrared band (MWIR, λ = 3–5 µm),

which carries radiation from hot objects. An additional requirement for optics in imaging systems is that the TIR radiation is directed without distortion of the incident wavefronts, which requires maximizing specularity.

We propose that a plasmonic nanoparticle-coated metal mirror could offer these optical functionalities in a reflective arrangement while overcoming the limitations of traditionally used optical components in the infrared. Our approach is based on the well-known phenomenon that metal nanoparticles undergo plasmonic oscillations when exposed to solar wavelengths, resulting in strong scattering and absorption of light (Figure 2A). This enables an ensemble of disordered plasmonic metal nanoparticles to act as an efficient solar absorber.[13-18] The longer thermal wavelengths, however, interact weakly with individual nanoparticles due to their small cross sections, causing the ensemble to behave as a weakly lossy or reflective effective medium, as can be seen in the scattering efficiencies plotted in Figure 2A. Thus, by backing a layer of disordered plasmonic nanoparticles with an intrinsically IR-reflective homogenous metal layer, one should be able to create a selective absorptance in the solar wavelengths and reflectance in the TIR. Indeed, ample evidence of this phenomenon is seen in the literature on plasmonic or ceramic-metal nanocomposite-based selective solar absorbers, which also harness the selective absorption of plasmonic nanoparticles. $^{[14,19-22]}$ While these past works lend strong support to the technical feasibility of fabricating the design, for imaging applications, the preservation or reconstructability of the incident TIR wavefront www.advancedsciencenews.com

& PHOTONICS REVIEWS

www.lpr-journal.org

is crucial. Reconstructing the incident wavefront, along with the use of selectively solar absorptive designs in imaging applications, remains unexplored.

We verified the specularity of reflections from disordered plasmonic nanoparticle films using FDTD simulations. Because of computational constraints, and since we intended to show an intuitive representation of the general concept rather than a quantitatively accurate example, we used 2D simulations, which were sufficiently representative of the 3D cases [23-26] for our purpose (SI, Section 2). As shown in Figure 2B, a film of freestanding plasmonic nanoparticles does exhibit a specular behavior at $\lambda = 4 \, \mu m$, implying a similar behavior for longer TIR wavelengths as well. It should be noted that the film itself has a small surface roughness $(< 1 \mu m)$ relative to the TIR wavelengths, which is necessary for a specular behavior (SI, Section 6). Notably, a film of nanoparticles with sizes $\approx 10^1$ nm and lower fill fraction (≈ 0.4) shows both specular reflectance and transmittance (Figure 2B, left panel), while one with nanoparticles with sizes $\approx 10^2$ nm and higher fill fraction (\approx 0.75) shows a specular reflectance (Figure 2B, right panel). The differing behaviors are attributable to nanoparticle sizes relative to the electromagnetic penetration depths ($\delta \approx 10$ nm) (SI, Section 2), as well as the metal fraction in the LWIR effective medium. Overall, the results indicate that when backed with a metal reflector, the film of disordered plasmonic metal nanoparticles can behave as a solar absorptive, TIR reflective optical filter. In our experimental implementation, we aim for a reflective design comprising a film of plasmonic nanoparticles on a metal substrate, which we call the plasmonic reflective filter (PRF).

2.2. Experimental Demonstration and Optical and Radiometric Characterizations

While a plasmonic reflective filter (PRF) can in principle be created by a variety of methods, [19-22] here, as a proof-of-concept, we choose what is perhaps the fastest and most convenient way of fabricating one - a galvanic displacement reaction-based dip-anddry technique, which Mandal et. al. demonstrated for selective solar absorbers. $^{[14]}$ In the particular example shown in Figure 3A, a PRF comprising copper (Cu) nanoparticles on zinc is produced by dipping a mechanically flattened and polished strip of zinc (Zn) in 12.5 mм aqueous copper (II) sulfate for 20s. During the charge transfer process of the galvanic displacement reaction, the zinc on the surface of the strip ionizes and the copper ions in solution deposit as nanoparticles on the strip. Figure 3B shows that the disordered nanoparticles, which are clusters with sizes < 200 nm, comprise features < 50 nm in size. The nanostructured layer is quite uniform and appears to have a surface height variation of ≈ 1 nanoparticle, or $\approx 0.2 \mu m$ (Figure \$7, Supporting Information), which, being 40–65x of the LWIR wavelengths, should yield a specular reflectance. From Figure 1B,D, it is immediately clear that the PRF is a selective solar absorber and specular TIR reflector. Qualitatively, this serves as a proof-of-concept of the PRF's functionality as a reflective filter for thermal imaging systems. We also characterized the optical properties of the PRF by spectrophotometry and interferometry. As shown in Figure 3C, in this particular embodiment, the PRF has a specular reflectance of 0.007 in the solar and 0.78 in the LWIR wavelengths. The total (diffuse) reflectances are a low 0.028 and high 0.83 respectively in the solar and LWIR, with the non-specular components being \approx 74% and 5% of the total. As noted later in the manuscript, this corresponds to a higher LWIR:solar selectivity than Ge optics and can be tuned further, for instance, to increase the LWIR yield.

The experimental results are consistent with the Miescattering behavior of plasmonic nanoparticles in the solar (Figure 2A, lower panel), and effective medium behavior in the TIR (Figure 2A,B) wavelengths. A similar behavior is observed in FDTD simulations of the nanoparticle clusters (Figure 3B), which indicates that the layer of disordered nanoparticles may have an intermediate behavior between the semi-transmissive and reflective regimes (Figure 2B and SI, Section 2). The \approx 5% non-specular reflectance in the LWIR is likely due to the surface roughness of the zinc substrate alone, as the copper nanoparticle layer likely has a deep-subwavelength thickness.^[14] As shown in Figure 3, both the solar and LWIR non-specular components can be conveniently filtered by adjusting distances between the PRF and the detector or by using apertures. For the purposes of imaging and sensing, therefore, the specular component is of relevance. In that regard, we note that the LWIR:solar yield ratio (i.e., the ratio of reflectances) is a high 110 ($\approx 0.78/0.008$). This is a useful indicator of the signal-to-noise ratio, which varies with the intensity of solar and LWIR irradiances incident on the imaging and sensing system.

We also investigated the quality of the optical wavefronts reflected by the PRF, and by extension, its surface quality, by Twyman-Green interferometry at $\lambda \approx 8.1 \ \mu m.^{[27]}$ The upper left panel of Figure 3D shows the interference pattern observed when the "test" and "reference" arms of the interferometer contain a PRF and a standard, vapor-deposited plane aluminum mirror respectively. The pattern is similar to that observed when both arms contain standard mirrors (Figure 3D, upper right panel), which indicates that the PRF has an optically smooth surface and reflects specularly in the LWIR wavelengths. Additionally, as a proof-of-concept, we also curved a PRF into a concave shape by impressing it with a standard convex mirror. The lower left panel of Figure 3D shows the interference pattern when the curved mirror is used as the test optic, which is qualitatively similar to the pattern obtained when a concave mirror is used (Figure 3D, lower right panel). Both the interferometric and spectrophotometric characterizations presented here are consistent with the simulations (Figure 2) and photo- or thermographic evidence (Figure 1D). Crucially, they also show that the PRF has a high LWIR yield and solar filtration capability - a requisite for IR detection systems - and preserves the quality of the reflected wavefronts - which is necessary for imaging. This makes the PRF suitable as both planar and curved optical components for imaging systems (Figure 3E).

In addition to optical characterizations, we performed comparative radiometric characterizations of the PRF's imaging capability by comparing direct thermographs of objects with those of their reflections from the PRF. This was based on the idea that any thermal noise or artifacts due to the PRF would manifest if the PRF was serially added to the optical configuration. A FLIR Boson Camera (640 × 512 pixel, $\lambda_{\rm range} \approx 7.5$ –14 µm) was used in the experiments. **Figure 4A** shows the variation in temperatures along the dotted lines (insets) across a plastic with ≈ 200 nm silver deposited on one side. We observe that the variations across the sharp boundary between the emissive plastic (bright) and the

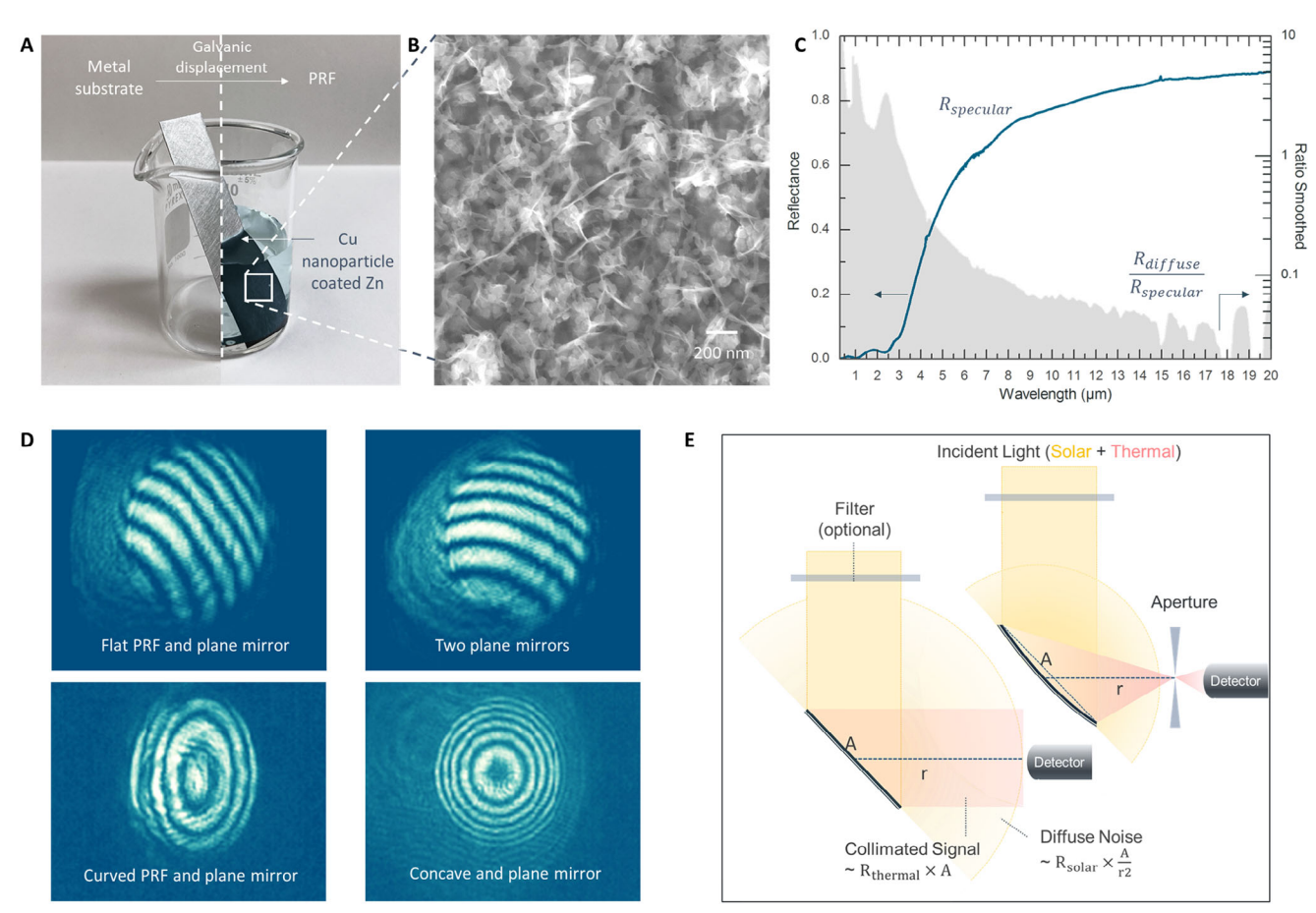


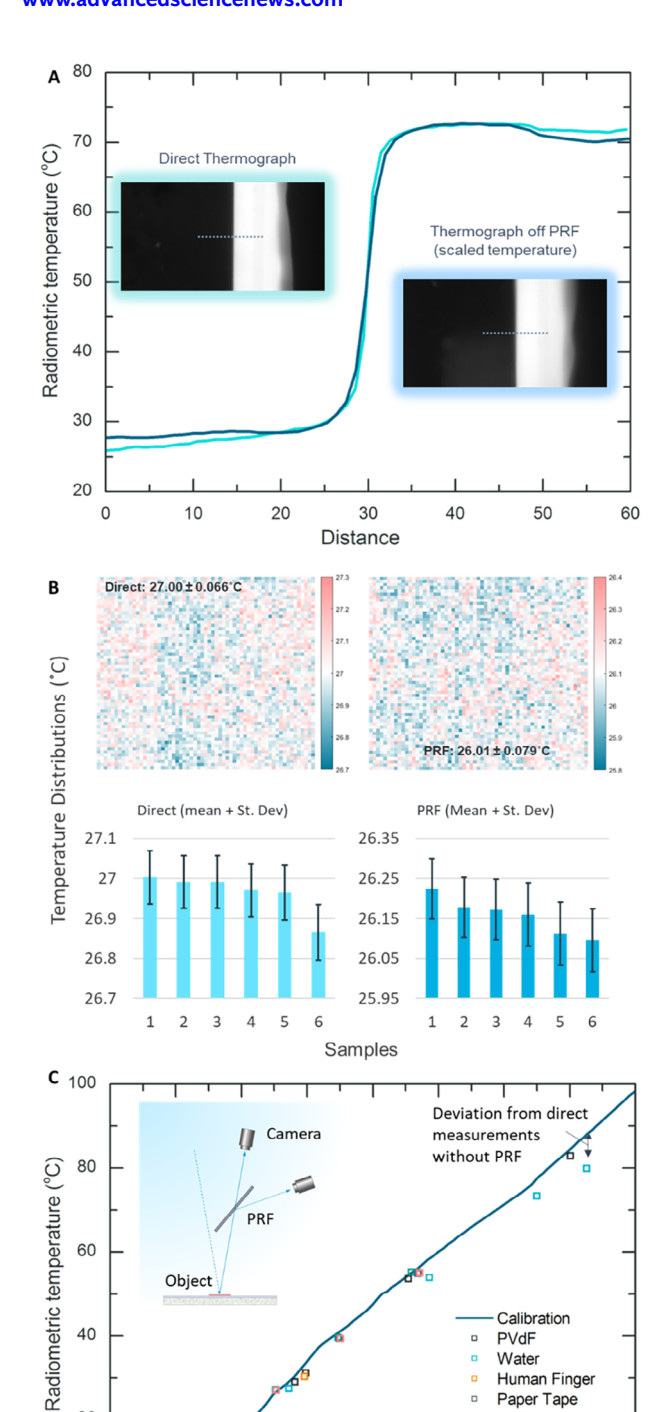
Figure 3. Experimental demonstration of a plasmonic reflective filter (PRF). A) Photograph showing a copper nanoparticle coated zinc foil, fabricated using a galvanic displacement reaction-based dip-and-dry technique. B) Scanning electron micrograph showing disordered copper nanoparticles on the zinc, with large ~200 nm clusters made from smaller nanostructures. C) Specular reflectance of a Cu-Zn PRF shown in blue, with the relative diffuse components shaded in grey. The fluctuation in the longer wavelengths is due to the noise in the diffuse reflectance data. As expected, reflection in the TIR is mostly specular, while that in the solar wavelengths is mostly diffuse. The specular/diffuse solar reflectances are 0.007 / 0.028, and LWIR reflectances are 0.784 / 0.833, respectively. D) (upper left) Twyman green interferogram obtained using a flat PRF and a plane optical grade mirror on the two interferometer arms. The presence of distinct fringes, and the similarities to the case for the two optical grade plane mirrors (upper right), indicate that reflection off the PRF is specular. The individual beams that produce the pattern in the top left panel, and an additional set of interferograms, are provided in Figure S3 (Supporting Information). Analogous interferograms for a roughly curved PRF (lower left) and a plane mirror, and a concave and plane mirror (lower right) show elliptical and circular fringes respectively, and indicate that the PRF could be formed into curved mirrors with focusing functionality as well. E) The results indicate that the PRF can be used as flat and focusing optics in IR sensing and imaging systems. Importantly, the non-specular noise can be filtered out, either by increasing the gap between the PRF and the detector or using apertures that are common in imaging systems. Additionally, filters can optionally be placed in front of the PRF to impart further optical selectivity.

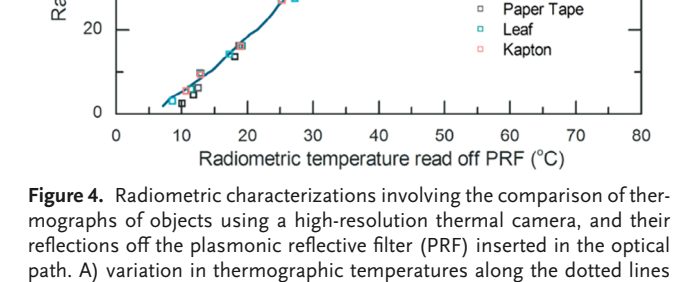
reflective silver (dark) are very similar, indicating that the insertion of the PRF in the optical path does not impact the sharpness of the image for the given camera resolution. This is promising, since the FLIR Boson 640 camera's 640 pixel \times 512 pixel resolution represents the higher end of thermographic capabilities for typical commercial applications. We also investigated whether the addition of a PRF as an imaging optic raises noise levels in thermographs. This was tested by placing a diffuse thermal emitter (paper with uniform thickness over double-sided Kapton tape) on a thick copper block, and taking multiple thermographs of a $\approx 1~{\rm cm}\times 1~{\rm cm}$ area of the emitter expected to have a uniform temperature at steady state, directly and off the PRF (SI, Section 1). Representative images are shown in Figure 4B. As shown, the direct image of the emitter has mean and standard deviations 26.965 \pm 0.066 °C. The image of the emitter taken off

the PRF has mean and standard deviations of 26.224 ± 0.079 °C. The higher noise levels for the image of the PRF are also observed in the other images taken (bar charts in Figure 4B) and indicate that the addition of the PRF does increase image noise levels by 0.01 K. However, the increase in noise is a fraction (\approx 16%) of the original, and the noise with the PRF is minute compared to temperatures typically measured by thermal cameras (\approx 230–420 K). Thus, additional noise arising from the PRF's use is unlikely to be significant.

As a further demonstration of the PRF's suitability for radiometry, we performed a preliminary calibration of the combined thermal camera + PRF system and used it to measure temperatures of common objects. The calibration was done by taking radiometric temperature measurements of a highly emissive roughened polyvinylidene difluoride film held at different

18638899, 2024, 9, Downloaded from https://onlinelibrary.wiley.com/doi/10.1002/por.202400256, Wiley Online Library on [02/03/2025]. See the Terms and Conditions (https://onlinelibrary.wiley.com/terms-and-conditions) on Wiley Online Library for rules of use; OA arctices are governed by the applicable Creative Commons License





(insets) across a plastic with ≈200 nm silver deposited on one side, show-

ing that the image sharpness is similar for both the direct and reflected (off

PRF) images. The latter was scaled to match the magnitude of the first.

B) (Top) Variation in radiometric temperature of an emitter designed to

temperatures from -5 to 105 °C directly with the thermal camera, and its reflection from the PRF at 50° angle of incidence (Figure 4C, inset). The results were then used to create a calibration curve that predicts the "real" temperature as would be recorded by the camera alone. The setup was then used to measure temperatures of a range of everyday objects (a leaf, paper, Kapton tape, human skin, a water drop, and smooth PVdF plastic) - both from the PRF and directly with the camera. The directly measured temperatures were then compared to the predictions based on the temperatures recorded using the PRF and the calibration curve. In all cases, potentially except for when the PRF was above the hot water drop, the temperature of the PRF was ≈20–22 °C (room temperature), which, given its low emittance, meant that its own thermal signature would be nearly constant across measurements, and could be ignored in this experiment.

As can be seen in Figure 4C, the measured and predicted radiometric temperatures show good agreement. We do note that in our demonstrations, the directly measured temperatures are often slightly (1-3 °C) lower than predictions based on the calibration, except for the large differences seen for water at high temperatures. The former is likely due to different ambient radiative temperatures for the calibration and the measurements, which can influence the reflected radiance from the objects being measured and the emitted radiance from the slightly emissive PRF. The latter was due to the heating of the PRF by the water vapor emanating from the hot water below it. These variations are expected, as compared to our rudimentary process, calibrations of radiometric systems are carried out in highly controlled and measured environments, and for multiple variables in addition to temperature. Nonetheless, the closeness of the prediction and the direct measurements indicate that PRFs integrated into thermal sensing systems can be used for radiometric measurements as well. This proof-of-concept demonstration thus lays the basis for advanced calibrations (with precisely controlled values of object, ambient, PRF, Ge-lens and camera core temperatures, humidities, and shortwave noise levels).

Lastly, we also tested the consistency and aging of the PRFs created using the galvanic displacement-based dip-and-dry fabrication method. As shown in the SI, Section 8, PRFs created using the same parameters and accounting for variations due to the manual nature of the process, yield near identical optical properties. Even such small variations could be eliminated if the process was mechanized and done at scale. Accelerated thermal aging of the PRFs at 100 °C for 96 h also shows a minute change in performance, indicating the long-term stability of the PRFs. Collectively, these results are promising for the PRF's real-life

have a spatially uniform temperature, showing fluctuations or noise levels about the mean for both the direct and reflected images. (bottom) Summarized results for multiple direct and reflected images. As shown, the noise levels for images taken with the PRF are marginally higher, but not significant. C) A preliminary radiometric calibration, performed by taking temperature measurements of an emissive target directly and off the PRF, yields quantitatively close predictions to temperatures measured directly using the thermal camera. Collectively, the results show the integrability of the PRF into thermal imaging and sensing systems without compromising their imaging or radiometric capabilities.

Calibratio

PV_{dF}

Water Human Finge

40



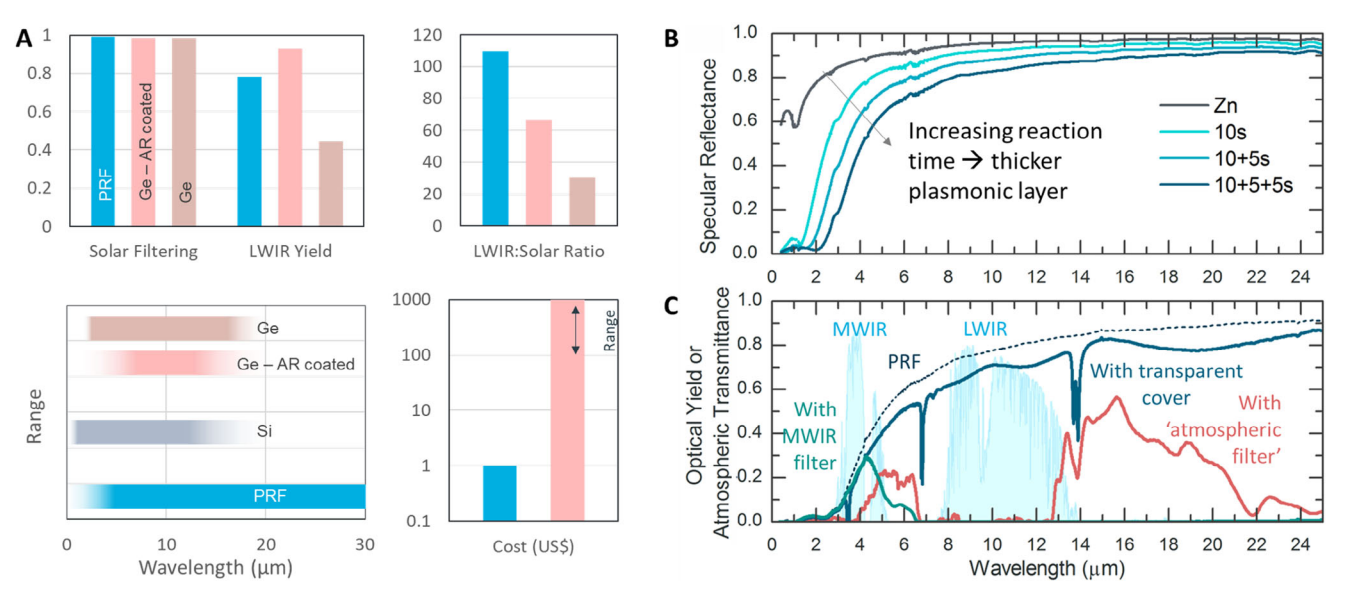


Figure 5. Comparisons of the PRF with state-of-the-art IR optics, and additional possibilities. A) Comparisons of the PRF's solar filtering, LWIR yield, ratio of LWIR signal to solar noise, wavelength range, and cost to those of Ge optics. [1] In general, the optical properties are comparable, but the PRF is created at orders of magnitude lower costs. B) Tunability of the spectral specular reflectance of the PRF, demonstrated here by varying reaction time of the aqueous copper (II) sulfate with zinc (Figure 3A). The corresponding parameters are presented in the SI, Section 7. This can be used for optimization of performance, for instance, for different wavelengths (e.g., MWIR or LWIR), or tuning the radiometric range of temperature measurement systems. C) Adding low-cost polymer or glass filters in front of the PRF (Figure 3E) can enable additional functionalities. Polyethene (blue curve) can provide protection, convective insulation, and lensing functionalities. Thin glass sheets (green curve) can enable MWIR selectivity. Selectively LWIR absorptive polymers used in radiative cooling applications [37–39] can enable an intriguing functionality where the PRF+filter system can selectively reflect atmospheric irradiance originating within a ≈1 km range onto detectors, which can enable the radiometric measurement of average temperatures across large distances.

3. Discussion

3.1. Comparison with State-of-the-art Thermal Optical Components

While we have demonstrated the plasmonic reflective filter's (PRF's) suitability for thermal imaging and sensing systems from an optical and radiometric perspective, ultimately, the adoption of this approach will depend on its benefits and limitations relative to state-of-the-art Ge-based optical components. We compare in Figure 5A the optical properties of the PRF and Ge-based transmission optics. As shown on the top-left panel, the specific PRF presented in Figure 1B, and 3C has a solar filtering capability similar to that of a 5 mm thick Ge optic, with the PRF's absorptance (0.972) and filterable non-specular reflectance (0.021) adding to 0.993 compared to the Ge-optic's 0.986. The PRF's LWIR yield in this specific case is a reflectance of 0.78, higher than germanium's (0.445) but lower than its antireflection-coated variant (0.928). However, the LWIR:solar selectivity of the PRF is higher in this specific case (Figure 5A, top-right panel), and it is noteworthy that the tunability of its spectral reflectance (Figure 5B) could be harnessed to enhance both the LWIR yield and the selectivity. Additionally, we also note that the monotonic variation in the spectral reflectance of the PRF, unlike the fluctuating transmittance of Ge beyond $\lambda \approx 11.5 \, \mu m$, can yield monotonically varying thermal signatures as a function of temperature, which can aid radiometric calibrations. Furthermore, the reflectance of the PRF stretches from $\lambda \approx 3 \,\mu \text{m}$ into the far-IR wavelengths ($\lambda > 25 \,\mu \text{m}$) (Figure 5A, bottom left panel). In contrast, germanium's transmittance is high across $\lambda \approx 2-16 \mu m$, while silicon's transmittance ranges across $\lambda \approx 1.2\text{--}14 \,\mu\text{m}$. The PRF is thus suitable for use over a wider infrared band.

Being a reflective design, the PRF also has characteristic optical advantages and disadvantages relative to transmissive Geoptics. One limitation is that reflective designs are less compact than transmissive ones. This could be overcome by using configurations similar to compact "mirror lens" designs for visible cameras. Such configurations have the disadvantage of a fixed camera aperture, i.e., no control over the depth of field.[29] However, any resulting blurriness in captured images may not be significant, as image sharpness in thermography is primarily limited by the detector array. On the other hand, a major benefit is that the PRF, with its thin nanoparticle layer on metal, is unlikely to suffer from the chromatic aberration that thick transmissive Ge-optics experience. Furthermore, unlike Ge, which undergoes free-carrier induced "thermal darkening" or opacity at temperatures above 65 $^{\circ}\text{C,}^{[4,28,30,31]}$ the PRF's optical dispersion and transmittance do not depend on temperature, and the example we created using the dip-and-dry method can withstand temperatures of up to 200 $^{\circ}\text{C}$ in air. $^{\text{[14]}}$ This can simplify radiometric considerations, and allow for a wider operating temperature range for thermal imaging and sensing systems.

The plasmonic reflective filter (PRF) is also fabricated by a convenient, low-cost, and versatile process. As demonstrated, the galvanic displacement reaction-based dip-and-dry method is a fast and highly convenient way of making PRFs. Given the generalizability of the method, it is compatible with a variety of widely available and low-cost metals (e.g., zinc, iron, galvanized www.advancedsciencenews.com

REVIEWS

www.lpr-journal.org

metals, brass, aluminum) and salt solutions (e.g., those of copper, iron, nickel, silver).[32-36] Additional processing involved molding the malleable and ductile zinc with a press, polishing it with sandpaper, and cleaning prior to the dip-and-dry process. We do note here that the electrochemical nature of the dip-and-dry process makes it sensitive to the grade and (in the case of the metal) surface finish of the reagents, as well as other variables that govern the surface reaction rate. However, these variables are well-understood and controllable. By comparison, the grinding of brittle Germanium optics,^[21] the material costs and thickness (≈5 mm) involved, and the application of antireflection coatings, all add to the cost of Ge-based optical components. Thus, while we made our PRFs at costs < US\$ 1, Ge-based optics cost in the US\$ 100-1000 range. The orders of magnitude difference in price persists even with the assumption that production costs are as low as ½ of the selling value.

The chemical synthesis of the PRF also allows an exceptional tunability of its spectral reflectance, which is not easily achievable through other approaches today. In the dip-and-dry technique we used, controlling reaction time allows for fine-tuning of the spectrum, while varying the reaction temperature and salt concentration can enable coarse tuning all the way from a selective solar absorber to a super-broadband absorber which absorbs well into the far-infrared.^[14,32] This is due to the dependence of the thickness and morphology (e.g., particle size distribution) of the nanoparticle coating on the reaction parameters.[14,32] An example of the variation in specular reflectance with reaction time is shown in Figure 5B. Besides optimizing for the LWIR yield, solar filtering, and their ratios (SI, Section 7), the tuning of spectral reflectance can be used to suppress the yield at MWIR wavelengths relative to the LWIR, or if MWIR filters are used (green curve in Figure 5C), optimize the MWIR yield. By comparison, the transmittances of Ge-optics are bound by the intrinsic absorptance of Ge. Optimization within those bounds is difficult to achieve for broad infrared bands using antireflection coatings, with typical designs reliant on advanced and expensive design and fabrication.

3.2. Outlook

In this work, we have demonstrated a disordered material-based plasmonic reflective filter that achieves a similar optical performance as state-of-the-art Ge-based optics, but for a fraction of the cost and through a vastly simpler fabrication process. Imaging in the visible and LWIR, spectrophotometry, and interferometry corroboratively indicate that the PRF has an efficient LWIR yield, solar filtering capability, and specular reflectance - requisites for thermal imaging and sensing systems. Thermographic and radiometric characterizations indicate that the PRF can be readily integrated into thermal imaging and sensing systems without compromising their performance. In practical terms, the 100-1000x reduction in cost, and the simplicity and versatility of the fabrication method represent a major advance. The former could be an overriding consideration in terms of use, as IR imaging and sensing expands into diverse, and potentially unforeseen applications (Figure S4, Supporting Information). However, we believe that the significance of this work goes beyond immediate practical ones, and could be the basis for further, meaningful explorations.

We first note that while surfaces with selective solar absorptance have been created for solar heating applications, this work is, to our knowledge, the first instance where their potential for imaging and sensing has been explored. As such, this work reports a previously unexplored optical functionality of disordered materials, and highlights the potential of disordered plasmonic media as a platform for the design of infrared optical components. Of perhaps greater significance is the fact that it was achieved using a chemical process that is unusual for optical design. We note that a wide array of chemical processes have been used to create plasmonic selective solar absorbers,[19,20,22,33,40,41] and could, in practice, be used to create PRFs (e.g., by electrodeposition of plasmonic nanoparticles on existing aluminum mirrors, or dealloying of gold ones) $^{[20,42-44]}$ as well. We, therefore, envision that this work will spur further exploration of non-traditional chemical fabrication pathways for novel, high-performance, and low-cost disordered optical designs. One exciting possibility would be transmissive designs containing nanoparticles embedded in a TIR transparent medium, since our simulations (Figure 2B) show that a thin film of small plasmonic nanoparticles at small fill fractions can be TIR transmissive. Another possibility would be to simultaneously optimize the solar filtering and LWIR yield of the PRF. The wide variety of materials and chemical fabrication platforms, [19,20,22,33,40,41] enable a wide range of pathways for structural optimization of the PRF's optical properties. It may also be possible to add solution-based anti-reflection coatings on the PRF. [45,46] Together, these open up a wide range of possibilities for increasing solar filtration and LWIR yield to near-perfect levels.

The chemical tunability of spectral reflectance of the PRF also raises the prospect of functionalities beyond what traditional IR imaging optics can achieve. One intriguing possibility is the control of the radiometric range of infrared imaging and sensing systems. It is well-known that the thermal radiance of objects being imaged increases with their temperatures, and if sufficiently high, it saturates or even burns infrared detectors. However, the spectral radiance also undergoes a blue shift with increasing temperature. Thus, a carefully designed decrease in the PRF's LWIR spectral reflectance toward shorter wavelengths (Figure 5B) can temper the increase in blue-shifted radiance. This can widen the range of temperatures measurable by thermal cameras, which are usually calibrated for narrow temperature ranges (e.g., -20 to 120 °C for typical LWIR cameras).

Lastly, we note that while we have primarily explored the PRF as an individual component for imaging applications, its solar filtering and broadband TIR reflectance allow it to be coupled with other scalable and spectrally selective filters (Figure 3E) for specific functionalities and applications (SI, Section 4). Figure 5C shows three possibilities. The blue curve represents the combined optical yield with a low-cost TIR-transparent polyethene filter, which can serve as a protective cover, a transparent lens, and, convective insulation for the imaging and sensing system. The green curve represents the optical yield when a glass microscope cover slip is used as a cover, which could be used for spectrally selective sensing in the MWIR wavelengths, which is often used for the detection of hot objects. Perhaps most intriguing is the example shown in red. In this example, a bilayer film of the polymers poly(4-methyl-1-pentene) and polyvinyl fluoride blocks out the LWIR and MWIR atmospheric transmission windows,

www.advancedsciencenews.com

www.lpr-journal.org

restricting the infrared yield of the TIR-reflective PRF to bands where the atmosphere radiates heat. In these bands, the atmosphere is typically opaque beyond ≈1 km, which offers the possibility of measuring the average ambient air temperatures across large distances. This could be realized by coupling the PRF + filter system with low-cost blackbody thermopile sensors. This is significant because currently, ambient temperatures are derived by spatially interpolating discrete measurements taken by weather stations or from vertical remote sensing by satellites. However, temperatures can vary greatly across short distances and satellites measure land surface temperatures.[47] By contrast, on-earth remote measurements of the effective mean air temperatures across large areas can offer more accurate values, which can be meaningful in fields like meteorology, climate modeling and forecasting, and thermal monitoring of urban environments.[48]

4. Experimental Section

Beyond the details in the manuscript, the Experimental Section is elaborated in the Supporting Information.

Supporting Information

Supporting Information is available from the Wiley Online Library or from the author.

Acknowledgements

J.M. was supported by Schmidt Science Fellows, in partnership with the Rhodes Trust. A.P.R. acknowledges support from the Alfred P. Sloan Foundation and the National Science Foundation under grant no. ECCS-2146577. J.B was supported by a National Science Foundation Graduate Research Fellowship under grants DGE-1650605 and DGE-2034835.

Conflict of Interest

The authors declare no conflict of interest.

Author Contributions

J.M. originated the concepts and created the PRFs. A.P.R. supervised the study. J.M. and A.P.R. designed the experiments. J.M. and J.B. performed optical characterizations. J.M. performed the thermographic and radiometric characterizations. J.M. and A.P.R. wrote the manuscript.

Data Availability Statement

The data that support the findings of this study are available from the corresponding author upon reasonable request.

Keywords

disordered, imaging, infrared, metamaterial, plasmonics

Received: February 25, 2024 Published online: May 28, 2024

- [1] Thorlabs. Germanium Windows. https://www.thorlabs.com/newgrouppage9.cfm?objectgroup_ID=3980.
- [2] Tydex. Tydex Germanium. http://www.tydexoptics.com/materials1/ for_transmission_optics/germanium/.
- [3] Crystran. Crystran Handbook of Optical Materials. https://www.crystran.co.uk/handbook.
- [4] Infrared Multilayer Laboratory. Germanium (Ge) University of Reading. https://www.reading.ac.uk/infrared/technical-library/cadmium-telluride-cdte/germanium-ge.
- [5] Chalcogenide Glasses: Preparation, Properties and Applications, (Eds: J.-L. Adam, X. Zhang), Woodhead Publishing, 2014.
- [6] M. Hubert, G. Delaizir, J. Monnier, C. Godart, H.-L. Ma, X.-H. Zhang, L. Calvez, Opt. Express 2011, 19, 23513.
- [7] J.-L. Adam, L. Calvez, J. Trolès, V. Nazabal, Int. J. Appl. Glass Sci. 2015, 6. 287.
- [8] D. H. Cha, H.-J. Kim, Y. Hwang, J. C. Jeong, J.-H. Kim, Appl. Opt. 2012, 51, 5649.
- [9] M. Meem, S. Banerji, A. Majumder, R. Menon, Broadband lightweight flat lenses for long-wave infrared imaging, PNAS, 2019, Vol. 116, pp. 21375–21378.
- [10] D. Ostrower, III-Vs Review 2006, 19, 24.
- [11] D. W. Peters, P. S. Davids, J. K. Kim, T. E. Beechem, S. W. Howell, D. Leonhardt, T. Ohta, J. R. Wendt, J. A. Montoya, in *Micro- and Nanotechnology Sensors, Systems, and Applications VII*, vol. 9467, International Society for Optics and Photonics, Bellingham, Washington 2015. p. 946729.
- [12] J. H. Vella, L. Huang, N. Eedugurala, K. S. Mayer, T. N. Ng, J. D. Azoulay, Sci. Adv. 2021, 7, eabg2418.
- [13] K. W. Boer, Advances in Solar Energy: An Annual Review of Research and Development Volume, Springer, New York 1986, 3.
- [14] J. Mandal, D. Wang, A. C. Overvig, N. N. Shi, D. Paley, A. Zangiabadi, Q. Cheng, K. Barmak, N. Yu, Y. Yang, Adv. Mater. 2017, 29, 1702156
- [15] P. Mao, C. Liu, F. Song, M. Han, S. A. Maier, S. Zhang, Nat. Commun. 2020, 11, 1538.
- [16] L. Zhou, Y. Tan, D. Ji, B. Zhu, P. Zhang, J. Xu, Q. Gan, Z. Yu, J. Zhu, Sci. Adv. 2016, 2, e1501227.
- [17] K. Bae, G. Kang, S. K. Cho, W. Park, K. Kim, W. J. Padilla, *Nat. Commun.* 2015, 6, 10103.
- [18] M. Zhu, Y. Li, F. Chen, X. Zhu, J. Dai, Y. Li, Z. Yang, X. Yan, J. Song, Y. Wang, E. Hitz, W. Luo, M. Lu, B. Yang, L. Hu, Adv. Energy Mater. 2018, 8, 1701028.
- [19] F. Cao, K. McEnaney, G. Chen, Z. Ren, Energy Environ. Sci. 2014, 7, 1615.
- [20] M. Chen, J. Mandal, Q. Ye, A. Li, Q. Cheng, T. Gong, T. Jin, Y. He, N. Yu, Y. Yang, ACS Appl. Energy Mater. 2019, 2, 6551.
- [21] P. Bermel, J. Lee, J. D. Joannopoulos, I. Celanovic, M. Soljačić, *Annu. Rev. Heat Transfer* **2012**, *15*.
- [22] C. E. Kennedy, Review of Mid- to High-Temperature Solar Selective Absorber Materials, https://www.osti.gov/biblio/15000706-review-mid-high-temperature-solar-selective-absorber-materials 2002 https://doi.org/10.2172/15000706.
- [23] M. Futamata, Y. Maruyama, M. Ishikawa, J. Phys. Chem. B 2003, 107, 7607.
- [24] E. Hao, G. C. Schatz, J. Chem. Phys. 2004, 120, 357.
- [25] T. Vo-Dinh, A. Dhawan, S. J. Norton, C. G. Khoury, H.-N. Wang, V. Misra, M. D. Gerhold, J. Phys. Chem. C 2010, 114, 7480.
- [26] J. Zhao, A. O. Pinchuk, J. M. McMahon, S. Li, L. K. Ausman, A. L. Atkinson, G. C. Schatz, Acc. Chem. Res. 2008, 41, 1710.
- [27] O. Kwon, J. C. Wyant, C. R. Hayslett, Appl Opt 1980, 19, 1862.
- [28] N. M. Ravindra, S. R. Marthi, A. Bañobre, Radiative Properties of Semiconductors, Morgan & Claypool Publishers, San Rafael, CA 2017.

2400256 (9 of 10)

© 2024 The Author(s). Laser & Photonics Reviews published by Wiley-VCH GmbH

& PHOTONICS REVIEWS

www.lpr-journal.org

www.advancedsciencenews.com

- [29] B&H. Mirror Lenses: Lightweight Super-Telephotos that Are Affordable | B&H eXplora. https://www.bhphotovideo.com/explora/photography/tips-and-solutions/mirror-lenses-lightweight-super-telephotos-that-are-affordable.
- [30] M. Schaub, J. Schwiegerling, E. Fest, R. H. Shepard, A. Symmons, Molded Optics: Design and Manufacture, CRC Press, Boca Raton, FL 2016
- [31] W. L. Fisba, E. Koontz, Germanium Alternative Gaining Momentum for IR Optics. https://www.photonics.com/Articles/Germanium_ Alternative_Gaining_Momentum_for_IR/a63146.
- [32] J. Mandal, Spectrally Selective Designs for Optical and Thermal Management, Columbia University, NY City 2019. https://doi.org/10.7916/ d8-0642-m193.
- [33] P. K. Gogna, K. L. Chopra, Sol. Energy 1979, 23, 405.
- [34] A. Gutés, C. Carraro, R. Maboudian, J. Am. Chem. Soc. 2010, 132, 1476.
- [35] D. A. Brevnov, T. S. Olson, G. P. López, P. Atanassov, J. Phys. Chem. B 2004, 108, 17531.
- [36] O. I. Kuntyi, H. I. Zozulya, O. Y.a. Dobrovets'ka, S. A. Kornii, O. V. Reshetnyak, *Mater. Sci.* 2018, 53, 488.
- [37] P. Grenier, Rev. Phys. Appl. 1979, 14, 87.

- [38] S. Catalanotti, V. Cuomo, G. Piro, D. Ruggi, V. Silvestrini, G. Troise, Sol. Energy 1975, 17, 83.
- [39] J. Mandal, S. Mandal, J. Brewer, A. Ramachandran, A. P. Raman, arXiv:2006.11931 2020.
- [40] T. Boström, E. Wäckelgård, G. Westin, Sol. Energy 2003, 74, 497.
- [41] C. M. Lampert, J. Washburn, Solar Energy Materials 1979, 1, 81.
- [42] P. Sondhi, K. J. Stine, Electrodeposition of Nanoporous Gold Thin Films, IntechOpen, London 2020. https://doi.org/10.5772/intechopen. 94604.
- [43] D. K. Sarfo, E. L. Izake, A. P. O'Mullane, G. A. Ayoko, Sens. Actuators, B 2018, 255, 1945.
- [44] R. D. Rivera-Rangel, M. E. Navarro-Segura, A. Arizmendi-Morquecho, M. Sánchez-Domínguez, Nanotechnology 2020, 31, 465605.
- [45] D. M. Bacal, N. N. Lal, A. N. Jumabekov, Q. Hou, Y. Hu, J. Lu, A. S. R. Chesman, U. Bach, Opt Express 2020, 28, 12650.
- [46] K. Askar, B. M. Phillips, X. Dou, J. Lopez, C. Smith, B. Jiang, P. Jiang, Opt Lett 2012, 37, 4380.
- [47] Z. S. Venter, T. Chakraborty, X. Lee, Sci. Adv. 2021, 7, eabb9569.
- [48] R. Napolitano, W. Reinhart, J. P. Gevaudan, Science 2021, 371, 1200.